CrystEngComm

Accepted Manuscript

ROYAL SOCIETY OF CHEMISTRY

www.rsc.org/crystengcomm

MnO_2 grafted V_2O_5 nanostructures: Formation mechanism, morphology and supercapacitive features

Balakrishnan Saravanakumar [a], Kamatchi Kamaraj Purushothaman [b], Gopalan Muralidharan [c*]

ABSTRACT

This article details an approach for fabrication of MnO_2 grafted V_2O_5 nanostructures to function as supercapacitor electrode. The MnO_2 and V_2O_5 combined and formed profitable hierarchical network morphology. Most importantly, both MnO_2 and V_2O_5 contributed to the energy storage. This kind of synergetic architecture exhibits the elevated specific capacitance (450 Fg^{-1} at 0.5 Ag^{-1}), good rate capacity (251 Fg^{-1} at 5 Ag^{-1}) and also provides better cycling stability (retaining 89% of capacitance after 500 cycles). An asymmetric supercapacitor using MnO_2 grafted V_2O_5 and activated carbon (AC) as electrodes was assembled. It exhibits specific capacitance of 61 Fg^{-1} with energy density of 8.5 $Whkg^{-1}$. The electrochemical feature lies in MnO_2 grafted V_2O_5 nanostructure is useful for the fabrication of high performance supercapacitor systems.

KEYWORDS: *Mixed oxide, V_2O_5 nanostructures, aqueous electrolyte*

---

[a] Faculty of Physics, Mahalingam College of Engineering and Technology, Pollachi, Tamilnadu, India. Tel: +91 9843867704, Email: saravanakumar123@gmail.com

[b] Faculty of Physics, TRP Engineering College (SRM Group), Irungalur, Trichy, Tamilnadu, India. Tel: +91 90035 92066 Email: purushoth_gri@yahoo.co.in

[c*] Department of Physics, Gandhigram Rural Institute, Deemed university, Gandhigram, Tamilnadu, India. Tel: +91451 2452371, Fax: +91 451 2454466, E-mail: muraligru@gmail.com

1. INTRODUCTION

Energy storage systems are greatly influenced in the process of advancing lifestyle of mankind. The speedy growth of mobile electronics and hybrid vehicles increased huge demand for power sources with high efficiency.[1] Among different kinds of power sources, the supercapacitor (SC), that can preserve and release large amount of electrical energy during very short span of time when it is needed.[2] SC is an appealing component, will be used to develop future hybrid electric vehicles (HEV) due to its unparalleled features like high power density, long cycle life, zero maintenance, environment friendliness and safety. It finds wide range of applications in our day to day life. SCs can provide an additional peak power in HEVs, load lifting equipments (forklift trucks, cargo cranes), mobile phones, camera (optical zoom and flash), uninterruptable power supplies, wind turbine blade pitching systems and etc.[3] Primarily a supercapacitor is composed of electrodes, separator and electrolyte. The innovative electrodes hold the key to determine the capacity, charge/ discharge rates and efficiency of a supercapacitor system.

It's of great significance to identify a versatile electrode material for achieving superior performance in supercapacitors. The vanadium pentoxide (V_2O_5) has always been fascinated since last decade owing to its layered structure, many oxidation states, abundance, non toxicity and low cost. In addition to that, V_2O_5 is a good intercalation compound and examined as an electrode material for energy storage applications like lithium ion batteries and supercapacitors.[4, 5] However so for, few reports have been reported in V_2O_5 for supercapacitor applications exclusively. The development of high performance supercapacitors with V_2O_5 as an electrode material is limited for its poor cycling stability, low electronic and ionic conductivity and slow electrochemical kinetics.

Presently, the use of nanostructured materials in supercapcitor electrodes holds interesting performance improvements. In bulk materials the interface between electrode and electrolyte significantly hamper the performance of the system.[6] Nanostructured materials include large number of electro active sites and it promotes surface activity of the electrode. The reduced dimensions of nano architectured materials allow effective electrolyte penetration facilitating fast electrode kinetics and excellent charge-discharge rates.[7]

In recent times, researchers fabricated different V_2O_5 nanostructures like nano hallow spheres, nanobelts, nanoflowers, nanowire, nanonetworks and etc.[8-12] Among these, nano networks are very attractive due to their structural richness. The network structure possess cross linking bridges and having multi dimensional voids. It facilities short ion diffusion channels and low resistive pathways, which gives more liberty for electrolyte penetration.[13, 14] Fabricating innovative network structured electrode materials with ample micro and meso pores greatly boosts the electrochemical performance of the supercapacitor system. The manganese oxide (MnO_2) having high value of theoretical capacitance 1100-1300 Fg^{-1}.[15] Also it is proved to achieve high experimental capacitance (600-800 Fg^{-1}) and better cycling stability up to thousands of cycles.[16, 17] Recently few admirable mixed oxide nanostructures for high specific capacitance and stability were reported. For instance, *Sarkar et al.* reported high performance capacitor electrodes based on α Fe_2O_3/ MnO_2 core−shell nanowire hetero structure arrays.[18] *Yang et al.* showed V_2O_5–TiO_2 nanotube arrays as supercapacitor electrodes.[19] *Cai et al.* demonstrated 3D Co_3O_4@$NiMoO_4$ core/shell nanowire arrays on Ni foam for electrochemical energy storage.[20] The utilization of aqueous electrolytes in energy storage systems are possess advantage of better safety, non flammability, low cost and shows higher power density compared to organic electrolytes.[21]

In this point of view, the strategy of uniting V_2O_5 nanostructures and Mn oxides may result fresh class of electrode material and expected to give synergetic electrochemical

performance. This design has the following special merits. (1) The MnO_2 and V_2O_5 are pseudocapacitive metal oxides having higher redox chemistry. Due to this, both the materials would effectively participate in the redox reaction involving electrolyte ions leading to the enhancement of specific capacitance. (2) The process of combining these materials into a nanostructure provides effective pathways and ensures the fast ion intercalation. (3) The presence of MnO_2 in V_2O_5 may act as a physical support and provides the better stability. To realize these ideas, we present a simple low cost strategy of blending MnO_2 with V_2O_5. The capping agent assisted co precipitation technique is adopted for preparation of MnO_2 grafted V_2O_5 nanostructures. This electrode design facilitates higher capacitance ($450Fg^{-1}$), better rate capacity at higher current rate ($251\ Fg^{-1}$ at $5\ Ag^{-1}$) and notable enhancement in cycling performance compared to pristine V_2O_5.

2. EXPERIMENTAL METHODS

All chemicals and materials were used directly without any further purification prior to use. Analytical grade vanadium pentoxide, hydrogen peroxide (30%) and potassium sulphate were purchased from SD Fine Chemicals Ltd., India. Potassium permanganate ($KMnO_4$) and manganese chloride ($MnCl_2$) were from Merck and disodium citrate was from Sigma Aldrich.

2.1 Synthesis of MnO_2 grafted V_2O_5

The V_2O_5 nano networks (VNN) are prepared by co precipitation technique as described elsewere.[12] Here we adopted modified co precipitation technique to fabricate MnO_2 grafted V_2O_5 nano architectures. In typical synthesis process of 5 wt% MnO_2 loading, 1.7289 g of V_2O_5 was added in to 375 ml of double distilled water (DDI). 15 ml of 30% H_2O_2 solution is slowly dropped (15 ml/min) to the V_2O_5 water mixture. The slurry started to bubble vigorously and change the color from yellow to orange. Subsequently 0.0218 g of $MnCl_2$ was dissolved in 10 ml of DDI. 0.0225 g of $KMnO_4$ was dissolved in 20 ml of DDI. Then the both solutions were

sonicated separately using ultrasonicator (LOBA life, 243 Hz) for 30 minutes. The as prepared $KMnO_4$ solution was added to V_2O_5 solution followed by slow dropping of $MnCl_2$ solution. Finally, disodium citrate was added as capping agent immediately under vigorous magnetic stirring at room temperature. The solution was stirred for 5 hrs to form a homogeneous mixture and aged for 3 days. The products were collected by centrifugation and dried at 100 °C for 10 h in a hot air oven to get final product. The mass percentage of V_2O_5, $KMnO_4$ and $MnCl_2$ was varied to prepare 5, 10 and 15 wt% loaded samples. The final products were denoted as VNM5, VNM10 and VNM15.

2.2 Characterization of MnO_2 grafted V_2O_5

MnO_2 grafted V_2O_5 nanostructures were characterized using X-ray diffraction (XRD) using a PANalytical X'pert- PRO diffractometer equipped with Cu Kα sealed tube (λ = 1.5406 Å). The sample was scanned in the range between 10 and 80° with a step size of 0.02° and exposure time of 10s. FTIR spectra were carried out using Perkin-Elmer Spectrum BX-II spectrophotometer using KBr pellets at room temperature. The Brunauer−Emmett−Teller (BET) method was used to calculate the specific surface area of the material. The nitrogen adsorption−desorption experiments were performed by Micrometeritics ASAP 2020 analyzer. The porosity distribution of the samples were produced from desorption branch of the isotherm using the Barrett− Joyner−Halenda (BJH) method. The morphologies of the materials were investigated using scanning electron microscopy (TESCAN VEGA 3 LMU scanning electron microscope) and transmission electron microscopy (TEM-Philips JEOL CM12). Energy dispersive spectra (EDS) of the samples were recorded using Bruker Quantax 200 AS instrument. Cyclic voltammetry (CV), galvanostatic charge−discharge (GCD), and electrochemical impedance spectroscopy (EIS) measurements were carried out using CHI 660 D electrochemical workstation (CH Instruments).

2.3 Preparation and evaluation of electrodes

Electrochemical investigations of MnO_2 grafted V_2O_5 samples were performed using a three-electrode cell set up, which consists of MnO_2 grafted V_2O_5 as working electrode, platinum wire as counter electrode, and Ag/AgCl as the reference electrode. A syrup of the electrode material was prepared by mixing 85 wt % sample , 10 wt % activated carbon (Sigma-Aldrich), and 5 wt % polytetrafluoroethylene (Sigma-Aldrich) with a few drops of ethanol. This semi liquid mixture was coated on 1 cm^2 nickel foam surface. It was followed by drying at 80 °C for 8 h to obtain the working electrode. Before coating, the Ni foam is cleaned with ultrasonic cleaner and dried in air for 1 hour. The electrochemical tests were carried out in 0.5 M K_2SO_4 aqueous electrolyte solution at atmospheric temperature. The specific capacitance and energy densities were calculated based on the mass of the active material (1 mg) in the electrode.

2.4 Fabrication of asymmetric supercapacitor assembly

An asymmetric type supercapacitor was assembled using MnO_2 grafted V_2O_5 nanostructures and activated carbon (Sigma-Aldrich, 1100 m^2/g) as electrode materials and polypropylene (Celgard, 2400) as a separator. Further 0.5 M K_2SO_4 utilized as electrolyte. CV and GCD measurements for asymmetric supercapacitor, was performed using CHI 660 D electrochemical workstation (CH Instruments).

3. RESULTS AND DISCUSSION

3.1 Analysis of structure and textural features

The purity and structure of the samples VNN, VNM2.5, VNM5, VNM10 and VNM15 were analyzed by X-ray diffraction (XRD) patterns as represented in the Fig. 1a. The existence of V_2O_5 peaks (marked as "*") affirms that the presence of orthorhombic nature (JCPDS card no. 41-1426, space group: Pmmn (59), a = 1.151 nm, b =0.356 nm, c =0. 437 nm) of V_2O_5 in the samples.[22] A notable peak broadening and reduction in intensity of the peaks is observed in

VNM2.5, VNM5 and VNM10 compared to VNN. The lack of strong intense peaks suggests that MnO_2 loading possibly reduces the crystalline nature of the sample. Further, the diffraction patterns of VNM15 shows good number of sharp V_2O_5 peaks. This may due to miscarriage of MnO_2 loading on V_2O_5. Similar trend like our work is reported by Ko and coworkers for ZrO_2/ V_2O_5 powders.[23] It is reasonable to expect, the absence of MnO_2 peaks in MnO_2 grafted samples owing to the very low MnO_2 mass percentage loading. The higher wt% of mass loading with V_2O_5 leads the change of its structure and it may alter the performance of the energy storage system.

Fig. 1b shows the FTIR spectra of VNN, VNM2.5, VNM5, VNM10 and VNM15 samples. The spectra present the distinctive bands that are attributable to V_2O_5. The band at 1018 cm^{-1} corresponds to V=O stretching mode. The band observed at 1615 cm^{-1} in all samples is attributed to bending vibrations of water molecules.[24] It is probably due to small traces of water molecules that got incorporated into the V_2O_5 during the formation process. The band at 829 cm^{-1} is referred to coupled vibration of V=O and V-O-V.[25] The inset of the Fig.1b represents magnified (400-800cm^{-1}) FTIR spectrum of VNM5. The band centered at 518 is cm^{-1} is attributed to the Mn-O stretching vibration.[26]

The morphology and structural newness of the VNN and MnO_2 grafted V_2O_5 samples were examined by scanning electron microscope (SEM) and transmission electron microscope (TEM). The SEM images of VNN (Fig S1), VNM2.5 (Fig S2) and VNM5 (Fig 2a) shows the presence of hierarchical interconnected network morphology. There is no obvious difference is noticed in the morphology of VNN, VNM2.5 and VNM5. Further, it confirms the sustainability of the interconnected network architecture after 2.5 and 5wt% MnO_2 mass loading. The high magnification SEM images of VNM5 (Fig. 2b and c) is also pronounced the existence of the network architecture. The presence of this kind of morphology in the materials is anticipated to provide better electrolyte ion transport and enhanced electrochemical performance.

The SEM images of MnO_2 loading with 10 Wt% are presented in the Fig. S3. The SEM images of VNM10 sample shows drastic change in the diameter of the voids present in the network. Further the SEM images of VNM15 (Fig. S3) distinctly confirm the destruction of network nature and turning to rough surface. It is evident that the weight percentage of MnO_2 loading on VNN plays an important role on the morphology of the material. Fig. 2d displays the energy dispersive spectra (EDS) and elemental mapping of VNM5 to validate the presence of Mn in the composite. The typical peaks of vanadium (V=32.75 Wt %), oxygen (O=63.3 Wt %) and manganese (Mn=3.93 Wt %) are found in EDS spectrum of VNM5. The elemental mapping images (Fig. 2 e, f, g) confirm the presence of V, O and Mn in the composite. Further, EDS line mapping spectrum is presented in Fig. S5. The overall signals (V, O and Mn) across the line trace (Insets of Fig. S5) is confirming the synergetic architecture of the material.

The TEM images of VNM5 is presented in the Fig. 3a, b and c. It shows the nano architecture of the material and showing the presence of voids and thin layer grafted over the V_2O_5. The selected area diffraction pattern (SAED) of VNM5 sample (inset of Fig. 3b) shows the ring pattern and absence of distinct diffraction spots. High resolution TEM image of VNM5 (Fig. 3d) reveals two different interplanar spacing ~0.7 nm and ~0.57 nm.[27, 28] It confirms a thin layer of MnO_2 coated over V_2O_5. This kind of morphology may endow the additional surface activeness and improve the electrochemical performance of VNM5 compared to VNN.

N_2 adsorption/ desorption isotherms were carried out to further understand the structural features of the sample. As shown in Fig. 4a, the nitrogen adsorption isotherm of MnO_2 grafted V_2O_5 nanostructures (VNM5) exhibits joined characteristics of type III/IV. The steep growth of nitrogen uptake at low pressure and loop structure confirms the presence of micro and meso pores in the sample. The measured BET surface area of VNM5 sample is 4.8 m^2g^{-1}. The pore size distribution (PSD) curve of the material is determined by BJH method. The pore diameter between 1-2 nm is denoted as micro pores and 2-50 nm as meso pores. From the Fig. 4b, PSD

curve maximum peaks observed at 1.4 nm, 2 nm, 2.7 nm and 4 nm. The presence of micropores with small mesopores in the active material effectively enhances the electrochemical behavior of the material.[13]

3.2 Growth mechanism of MnO_2 grafted V_2O_5

Different properties are accountable for the final morphology of the yield. Normally the source of the architecture is from energies associated with nucleation process, species encircling the surface and saturation level of the ingredients used. We endeavour to explain the possible growth mechanism of MnO_2 grafted V_2O_5 nanostructures. Fig. 5 elucidates the formation scheme of MnO_2 grafted V_2O_5 nano architectures. From past decade H_2O_2 is used as an oxidative agent /etchant for surface modifications of the materials. The use of H_2O_2 to form micro and meso pores has been reported by many research groups.[29, 30] Initially appropriate amount of H_2O_2 blended with V_2O_5 and H_2O. Due to the good association of V_2O_5, H_2O_2 and H_2O the solution commences many chemical reactions synchronously. The yellow colored solution changed to orange and then to wine red. This change in color is due to the formation of diperoxovandate and mono peroxovandate cations.[31] The saturation condition of the solution favors the nucleation process. The addition of $KMnO_4$ and $MnCl_2$ trigger the formation of MnO_2. In nano reign, the joining of particles greatly reduces surface energy coupled with unsatisfied chemical bonds.[32] Because of thermodynamics instability and high surface energy, the MnO_2 starts to attach with V_2O_5 and reduces the surface energy. The steady reaction process leads the growth of MnO_2 over V_2O_5. The presence of MnO_2 on V_2O_5 is visible in the TEM images of VNM5 as shown in Fig. 3.

3.3 Structural consequence of MnO_2 loading level

The morphology of VNM5 includes the unusual structural features like well specified hallow interior, 2D building blocks and inter connected networks which are benefit to enhance the electrolyte penetration with improved electrochemical features. The percentage mass loading

of MnO_2 plays a critical role in the unique morphology of the sample. A panoramic view of SEM images of VNM2.5 and VNM5 samples reveals that there is no considerable change of network architecture and it probably resembles the network morphology of VNN. It suggests the low percentage MnO_2 mass loading on VNN does not affect the network morphology of the sample. In this point of view, further increment of MnO_2 loading level seem to affect the interconnected network nature of the material. The SEM micrographs of VNM10 sample shows the change of void dimensions in the network structure. Moreover the increased addition of MnO_2 (15wt%) firmly crash the network feature of the sample and results into densely packed surfaces which is distinctly visible in SEM images(Fig. S4). The higher weight percentage MnO_2 loading seriously diminishes beneficial morphology of the sample. The low weight percentage loading is highly favorable for enhanced electrochemical performance. The VNM5 sample is more focused in further electrochemical investigations due to the advantageous morphological features lies in the material.

3.4 Energy storage in MnO_2 grafted V_2O_5

To explore the existence of electrochemical features of VNN and MnO_2 grafted V_2O_5 nanostructures, cyclic voltammetry (CV) test was accomplished between a potential ranges of 0 to 1V at the scan rate of 2 mVs^{-1}. The CV curves in Fig. 6a shows the presence of redox peak, which suggests that the specific capacitance arises mainly due to fast faradic reaction. The specific capacitance of the electrode from CV measurements can be obtained according to the following equation,

$$C = \frac{i}{v \times m} \qquad \text{----------(1)}$$

Where C (Fg^{-1}) is the specific capacitance, m (mg) is the mass of the active material in the electrode, i (mA) is the average current during anodic and cathodic scan and v (v) is the voltage sweep rate. The calculated specific capacitance values from CV measurements are 326, 364,

417, 232 and 113 Fg^{-1} for VNN, VNM2.5, VNM5, VNM10 and VNM15 respectively. Interestingly, as expected VNM2.5 and VNN5 sample exhibits improved specific capacitance compared to VNN and also VNM10, VNM15. The VNM5 electrode shows 28% increased specific capacitance compared to VNN**.** It is worth to mention here that the presence of MnO_2 with V_2O_5 network structure provides good surface kinetics of the material. The network structure of V_2O_5 creates effective channels for electrolyte ion penetration. This high capacitance benefit of VNM5 is due to synergetic effect of MnO_2 and network structured V_2O_5. In contrast to this elevated capacitance of VNM5, remarkable decrease of specific capacitance is observed in VNM10 and VNM15 with increased weight percentage loading. The rise of weight percentage of MnO_2 in the electrode leads the dense packing and provides only confined channels for electrolyte ion penetration. This high loading unusually grows the contact resistance and harms the specific capacitance.[33, 34] This probably results in poor capacitances in the case of samples containing 10 and 15 wt% of MnO_2.

Fig. 6b shows the CV curves of VNM5 with different scan rates. The linear growth of anodic/ cathodic current peak with increase of scan rate reflects that the redox process is diffusion controlled process and it ensures the better reversibility of redox reactions.[19] Fig. S6 shows the specific capacitance as a function of scan rate. It shows increase of scan rate reduces the specific capacitance.

Rate capacity plays a key role in the process of making high performance supercapacitors. The galvanostatic charge/ discharge (GCD) curves of VNN and MnO_2 loaded V_2O_5 samples at the constant current density of 0.5 Ag^{-1} between -0.2 to 0.8 V are shown in Fig. 7a. Further the GCD profiles are appreciated to draw supercapacitor features such as specific capacitance and rate performance. The discharge specific capacitance can be calculated from the discharge curves by applying following relation,

$$C = \frac{I \times \Delta t}{m \times \Delta v} \quad \text{---------- (2)}$$

Where I (mA), Δt (s), Δv (V) and m (mg) are the discharge current, time needed for discharge in the potential range of Δv and mass of the active material in the electrode. The calculated discharge specific capacitance values are 314, 373, 450, 268 and 118 Fg^{-1} for VNN, VNM2.5 VNM5, VNM10 and VNM15 respectively. The VNM2.5 and VNM5 samples show enhanced specific capacitance compare to VNN like CV measurements. Here it is valuable to note, VNM5 offers nearly 43 % increase in specific capacitance compared to VNN at this current density. This superior capacitance enhancement is mainly attributed to the synergetic effect of V_2O_5 and MnO_2 with network morphology. Fig. S7 shows the GCD curves of the samples with different current densities. These curves display the quasi triangular and symmetric in nature with a thin voltage iR drop. This confirms the superior charge/ discharge reversibility.

Fig. 7b shows the variation of specific capacitance with different current densities. Here it is noted that the increase of current density reduces the specific capacitance. At low current density, the electrolyte ions have enough time to intercalate with active material in the electrode. It effectively utilizes inner sites of active materials present in the electrode and significantly improves the specific capacitance. At higher current densities, no ample time for electrolyte ion to penetrate into active material. Thus the ions accessed only exterior part of the active material and diminish the specific capacitance.[35] In addition to these profitable features of VNM5, it shows the specific capacitance of 251 Fg^{-1} at the current density of 5 Ag^{-1}. This confirms the better rate capacity of the VNM5 electrode. The better withstanding capacity of VNM5 at higher scan rates makes this material as more attractive for energy storage applications.

To further show the advantage of this synergistic electrode design the cyclic stability test was carried out. Fig. 8a shows the cyclic life test of VNM5 for 500 cycles at a current density of 10 Ag^{-1}. The VNM5 electrode shows 89 % capacity retention up to 500 cycles. Here, the limited

cyclic stability of VNM5 stands a critical concern. Specifically at nano scale, the deformation of the active material by charge/discharge process. But VNM5 shows better cyclic stability compared to some of the recent reports. For instance, *Qu et al.* reported capacity retention upto 100 cycles for $V_2O_5.0.6H_2O$ nanoribbons. [36] *Perera et al* showed the stability upto 50 cycles for Vanadium oxide nanotube spherical clusters prepared on carbon fabrics. [37] *Perera et al.* displayed cyclic stability (70%) up to 70 cycles for vanadium oxide nanowire/ graphene composites. [38]

The electrochemical impedance spectroscopy (EIS) analysis was conducted for better understanding of structure and interfacial behavior of electrodes. The Nyquist plot for VNN, VNM5, VNM10 and VNM15 in the frequency range of 0.01 Hz to 100 KHz is shown in the Fig. 8b. The Nyquist plot is represented by an equivalent circuit model as shown Fig. S8. In the equivalent circuit, ohmic resistance of the electrolyte is denoted as Rs. R_{CT} is the charge transfer resistance connected parallel with double layer capacitance C_{DL} to represent the lower left segment of the curve is marked as the higher frequency region. The semi circle present in the high frequency region is due to charge transfer resistance (R_{CT}) between electrode and electrolyte. The magnified view of high frequency region is presented in inset of Fig 8b. The measured R_{CT} values for VNN, VNM2.5, VNM5, VNM10 and VNM15 are 1.68, 1.9, 2.22, 2.63 and 4.22 Ω respectively. The low values of R_{ct} manifesting the low internal resistance and enhanced conductivity of the electrode. The inclination of the spectra with real axis is due to leakage resistance (R_L) associated with mass capacitance C_L. It is noted that the vertical lines nearly parallel to the imaginary axis indicate the ideal capacitive behavior of the electrodes.

3.5 Asymmetric supercapacitors

To evaluate the performance of a full cell supercapacitor, we assembled a asymmetric supercapacitor using VNM5 and activated carbon (AC) as electrode materials. The capacitive features of the VNM5 // AC asymmetric supercapacitor, is displayed in the Fig. 9. The Fig. 9a

shows the CV curves of VNM5 // AC at the scan rate of 2 mVs^{-1} in the potential window of 0 to 1V in 0.5M K_2SO_4 electrolyte. The rectangular shape of the CV curve indicates the capacitor behavior. CV curves of VNM5 // AC at different scan rate is displayed in the Fig. 9b. It confirms the better reversibility of VNM5 // AC asymmetric supercapacitor over different scan rates. Fig. 9c shows the GCD curve for VNM5 // AC at the current density of 0.5 Ag^{-1}. The rectangular shaped GCD curve further indicates the capacitive nature. The GCD curves at different current densities also displayed in the Fig. 9d. The calculated specific capacitance of VNM5// AC asymmetric supercapacitor at 0.5, 1, 1.5 and 2 Ag^{-1} are 61, 48, 42, 38 Fg^{-1} respectively. The calculation of energy and power densities from 2 electrode system is more appropriate than 3 electrode system.[39] The following equations were adopted to calculate the energy and power density values.

$$E = \frac{1}{2} C_{\text{Cell}} (\Delta V)^2 \qquad \text{----------(3)}$$

$$P = \frac{E}{t} \qquad \text{----------(4)}$$

Where C_{Cell} (Fg^{-1}), Δv (V), E ($Whkg^{-1}$), P(Wkg^{-1}) and t(s) are the specific capacitance from two electrode system, potential window of discharge, energy density, power density and time respectively. The VNM5 // AC asymmetric supercapacitor exhibits the energy density of 8.5 Wh kg^{-1} and a power density 127 Wkg^{-1}. Fig. S7 presents the Ragone plot of VNM5 // AC asymmetric supercapacitor shows the variation of energy density with respect to power density.

4. CONCLUSIONS

In conclusion, we proposed a simple and cost effective approach to produce nano architectures for supercapacitor electrode applications. Structural investigations on MnO_2 grafted V_2O_5 nanostructures reveal the sustainability of network morphology even after MnO_2 loading. The smart MnO_2 grafted V_2O_5 nanostructured electrodes exhibits much better specific capacitance, rate capacity and stability compared to pristine V_2O_5. This enhanced performance is ascribed to the synergetic effect of MnO_2 and V_2O_5 with ordered nano network structure. Further VNM5// AC asymmetric supercapacitor was assembled and its performance also reported. The high performance of MnO_2/ V_2O_5 design can be utilized as electrodes towards super capacitor systems. The simplicity of this design can be generalized to other materials to make new multifunctional electrode materials.

Electronic Supporting Information (ESI): SEM and TEM images of VNN, SEM images of VNM2.5, VNM10 and VNM15 with different magnifications. EDS line scanning of VNM5. Variation of specific capacitance with various scan rate from CV measurements. Charge/ discharge curves of VNN, VNM2.5 VNM5, VNM10 and VNM15 with different current densities. Equivalent circuit model and Ragone plot for VNM5 // AC asymmetric supercapacitor.

REFERENCES

1. W. W. Liu, Y. Q. Feng, X. B Yan, J. T. Chen, Q. J. Xue, *Adv. Funct. Mater.*, 2013, 23, 4111-4122.

2. B. G. Choi, J. Hong, W. H. Hong, P. T. Hammond, H. Park, *ACS Nano.,* 2011, 5(9), 7205-7213.

3. P. J. Hall, M. Mirzaeian, S. I .Fletcher, F. B. Sillars, A. J. R. Rennie, G. O. Shitta-Bey, G. Wilson, A. Cruden, R. Carter, *Energy Environ. Sci.*, 2010, 3, 1238-1251.

4. X. Rui, Z. Lu, H. Yu, D. Yang, H. H. Hng, T. M. Lim, Q. Yan, *Nanoscale.*, 2013, 5, 556-560.

5. G. Wee, H. Z. Soh, Y. L. Cheah, S. G. Mhaisalkar, M. Srinivasan, *J. Mater. Chem*., 2010, 20, 6720-6725.

6. S. Chen, W. Xing, J. Duan, X. Hu, S. Z. Qiao, *J. Mater. Chem. A.*, 2013, 1, 2941-2954.

7. P. Balaya, *Energy Environ. Sci.,* 2008, 1, 645-654.

8. M. Wu, X. Zhang, S Gao, X. Cheng, Z. Rong, Y. Xu, H. Zhao, L. Huo *CrystEngComm*, 2013,15, 10123-10131.

9. M. Li, F. Kong, H. Wang, G. Li, *CrystEngComm*, 2011,13, 5317-5320.

10. M. R. Parida, C. Vijayan, C. S. Rout, S. C. Sandeep, R. Philip, P. C. Deshmukh. *J. Phys. Chem*. C 2011, 115, 112.

11. A. Pan, J. G. Zhang, Z.Nie, G. Cao, B. W. Arey, G. Li, S. Liang, J. Liu, *J. Mater. Chem.*, 2010, 20, 9193-9199.

12. B. Saravanakumar, K. K. Purushothaman, G. Muralidharan, *ACS Appl. Mater. Interfaces* 2012, 4, 484−4490.

13. Y. Liang, F. Liang, H. Zhong, Z. Li, R. Fu, D. Wu, *J. Mater. Chem. A.,* 2013, 1, 7000-7005.

14. H. Zhong, F. Xu, Z. Li, R. Fu, D. Wu, *Nanoscale.*, 2013, 5, 4678-4682.

15. G. Wang, L. Zhang, Zhang, J. *Chem. Soc. Rev,* 2012, 41, 797-828.

16. Y. Huang, Y. Li, Z. Hu, G. Wei, J. Guo, J. Liu, *J. Mater. Chem. A.*, 2013, 1, 9809-9813.

17. K. Kai, Y. Kobayashi, Y. Yamada, K. Miyazaki, T. Abe, Y. Uchimoto, H. Kageyama, *J. Mater. Chem.*, *2012, 22, 14690-14695.*

18. D. Sarkar, G. G. Khan, A. K. Singh, K. Mandal. *J. Phys. Chem. C,* 2013, 117, 15523-15531.

19. Y. Yang, D. Kim, M. Yang, P. Schmuki, *Chem. Commun.,* 2011, 47, 7746-7748.

20. D.Cai, D. Wang, B. Liu, L. Wang, Y. Liu, H. Li, Y. Wang, Q. Li, T. Wang. *ACS Appl. Mater. Interfaces.,* 2014, 6, 5050-5055.

21. Q. T. Qu, P. Zhang, B. Wang, Y. H. Chen, S. Tian, Y. P. Wu, R. J. Holze, *J. Phys. Chem. C* 2009, 113, 14020- 14027.

22. B. H. Kim, K. S. Yang, D. J. Yang, *Electrochim Acta, 2013,* 109, 859-865.

23. Y. N. Ko, S. H. Choi, Y. C. Kang, S. B. Par, *ACS Appl. Mater. Interface.*, 2013, **5**, 3234-3240.

24. G. Qiu, S. Dharmarathna, H. Genuino, Y. Zhang, H. Huang, S. L. Suib, *ACS Catal.*, 2011, 1, 1702-1709.

25. J. Zhu, J. He. ACS Appl. Mater. Interfaces 2012, 4, 1770−1776.

26. J. Yang, T. Lan, J. Liu, Y. Song, M. Wei, *Electrochim Acta.,* 2013*, 105,* 489-495.

27. A. Sakunthala, M. V. Reddy, S. Selvasekarapandian, B. V. R. Chowdari , P. Christopher Selvin, *Energy Environ. Sci.,* 2011, 4, 1712- 1725.

28. J. Yan, Z. Fan, T. Wei, W. Qian, M. Zhang, F. Wei. *Carbon,* 2010, 48, 3825-3833.

29. M. V. Vasylyev, R. Neumann, *J. Am. Chem. Soc.* 2004, 126, 884-890.

30. X. Zhong, Y. Qu, Y. C. Lin, L. Liao, X. F. Duan, *ACS Appl. Mater. Interfaces.* 2011, 3, 261-270.

31. Y. Liu, M. Clark, Q. Zhang, D. Yu, D. Liu, J. Liu, G. Cao, *Adv. Energy Mater.*2011, 1, 194-202.

32. L. Q. Mai, F. Yang, Y. L. Zhao, X. Xu, L. Xu, Y. Z. Luo, *Nat.Commun.*, 2011, 2, 381, DOI: 0.1038/ncomms1387.

33. L. Bao, J. Zang, X. Li, *Nano Lett.*, 2011, 11, 1215-1220.

34. Y. Hou, Y. Cheng, T. Hobson, J. Liu, *Nano Lett.*, 2010, 10, 2727-2733.

35. L. Wang, H. Ji, S. Wang, L. Kong, X. Jiang, G. Yang, *Nanoscale.*, 2013, 5, 3793-3799.

36. Q. T. Qu, Y. Shi, L. L. Li,W. L. Guo, Y. P. Wu, H. P. Zhang, S. Y. Guan, R. Holze, *Electrochem. Commun*. 2009, 11, 1325-1328.

37. S. D. Perera, B. Patel, J. Bonso, M. Grunewald, J. P. Ferraris, K. J. Balkus, Jr. *ACS Appl. Mater. Interfaces.*, 2011, 3, 4512-4517.

38. S. D. Perera, A. D. Liyanage, N. Nijem, J. P. Ferraris, Y. J. Chabal , K. J. Balkus, Jr. *Journal of Power Sources.*, 2013, 230, 130-137.

39. M. D. Stoller, R. S. Ruoff. *Energy Environ. Sci.,* 2010, 3, 1294- 1301.

FIGURES AND CAPTIONS

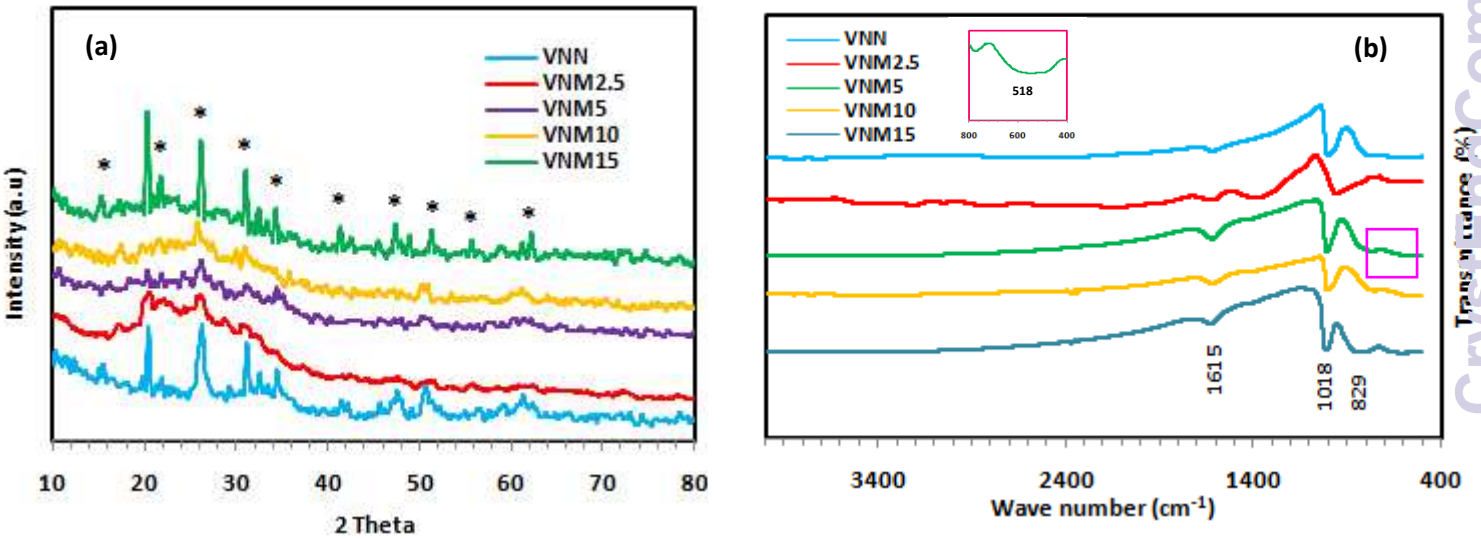

Fig.1. (a) XRD patterns of VNN, VNM2.5, VNM5, VNM10, and VNM15. (b) FTIR spectra for VNN, VNM2.5, VNM5, VNM10, and VNM15. Inset of Fig.1b shows the magnified FITR spectra for VNM5.

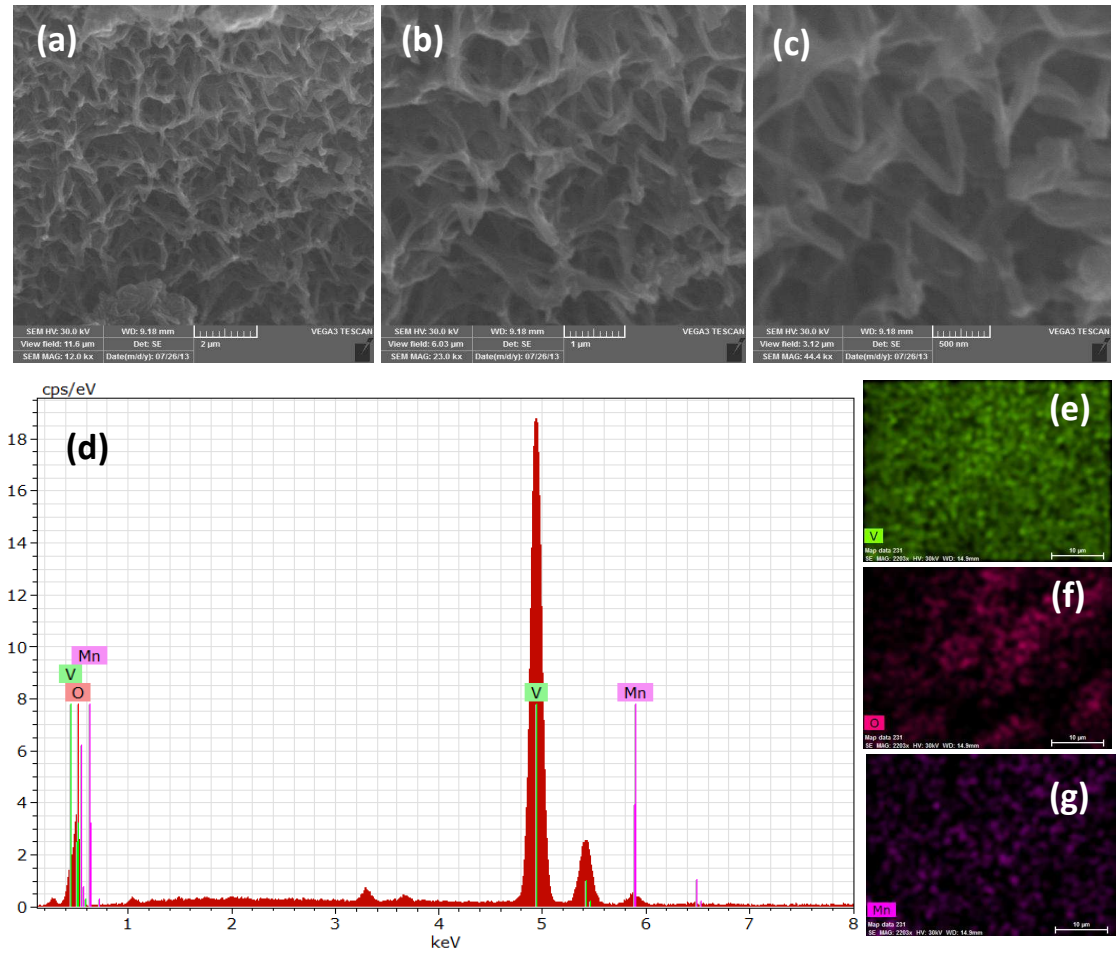

Fig. 2(a, b, c) SEM images of VNM5 with different magnifications (x12000), (x23000), (x44000). (d) EDS spectra of VNM5 (e, f and g) elemental mapping images of V, O and Mn.

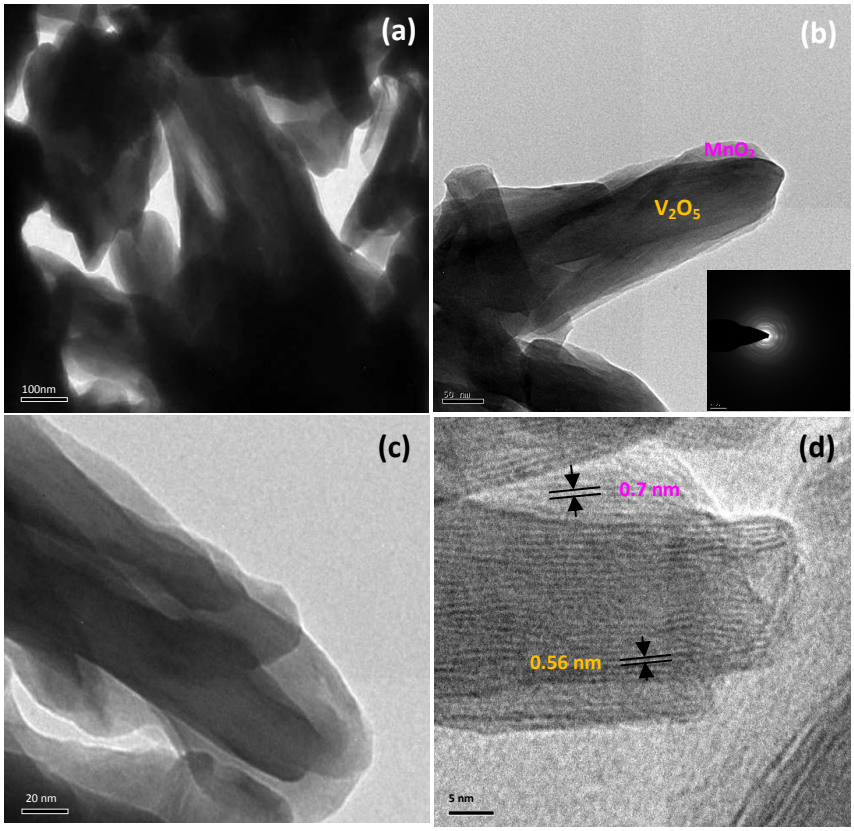

Fig. 3 (a, b, c) TEM images of VNM5. Inset of Fig. 3b showing SAED pattern of VNM5. (d) High resolution TEM image of VNM5.

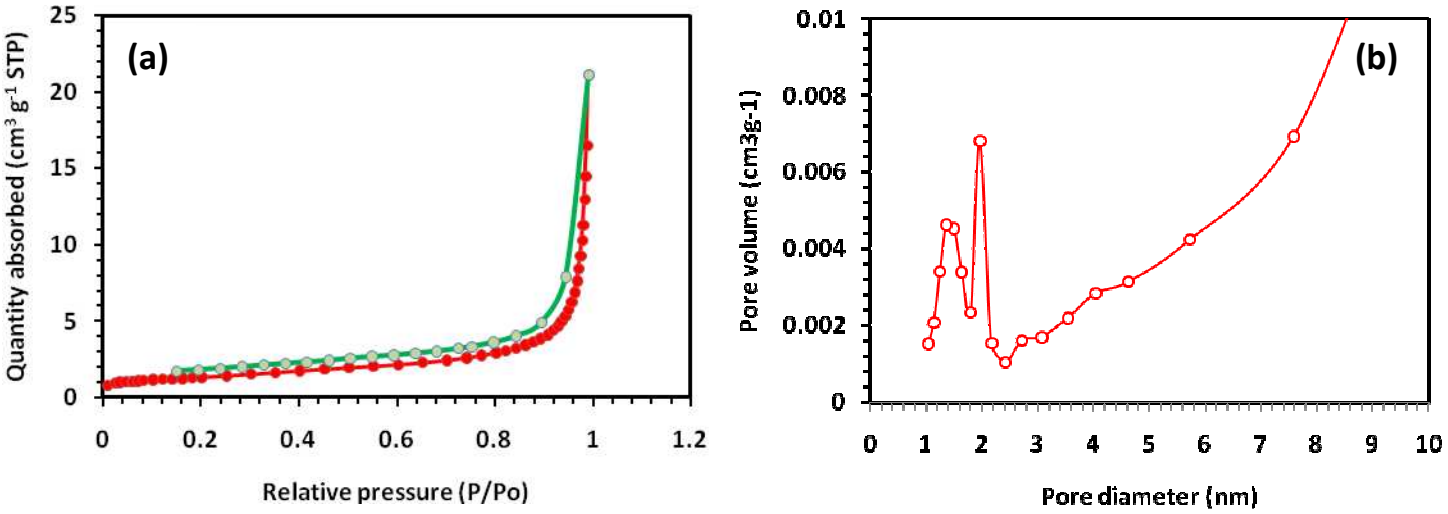

Fig. 4a Nitrogen adsorption−desorption isotherm of VNM5. (b) The pore-size distribution of VNM5.

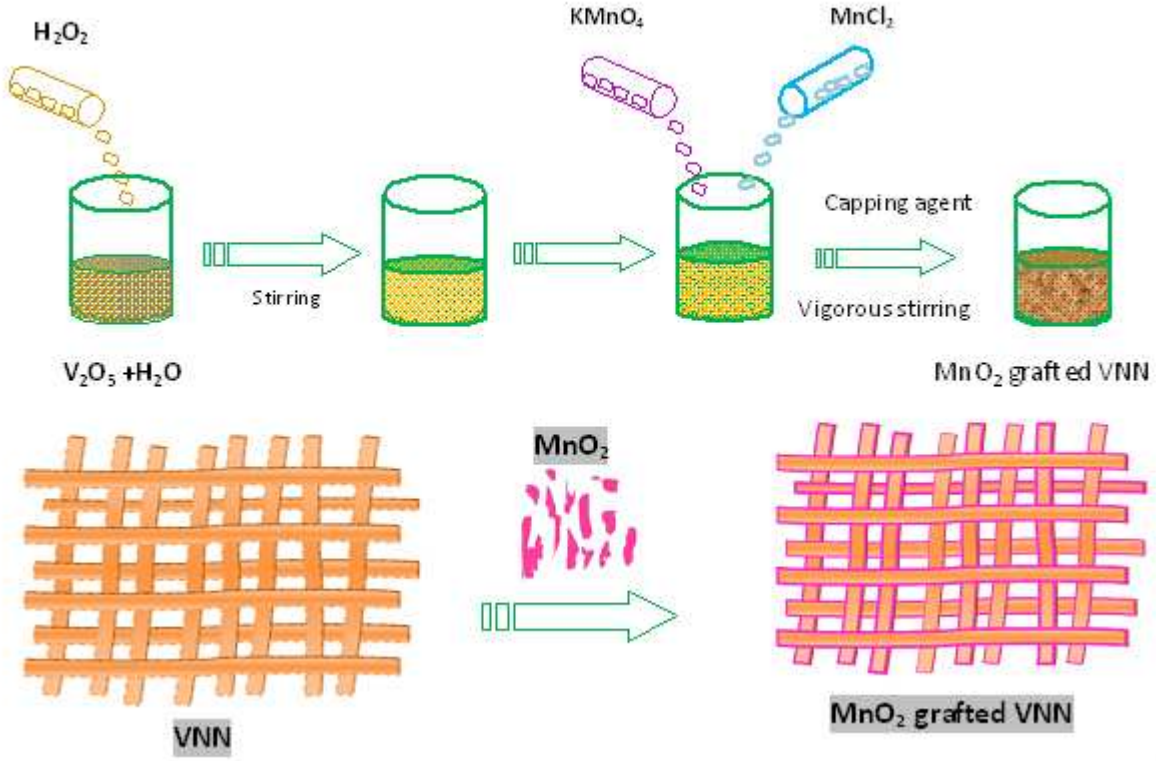

Fig. 5 The formation mechanism of MnO_2 grafted V_2O_5 nano architectures.

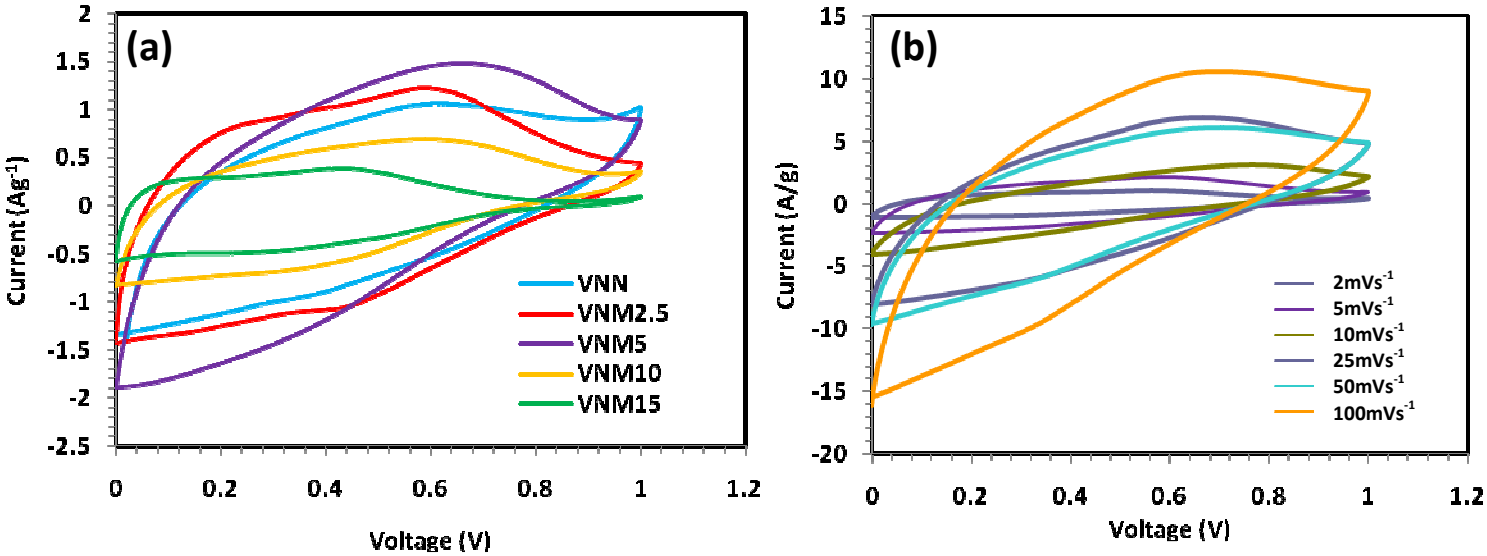

Fig. 6(a) CV curves of VNN, VNM2.5, VNM5, VNM10, and VNM15 measured at $2mVs^{-1}$ (vsAg/AgCl). (b) CV curves of VNM5 measured at different scan rates.

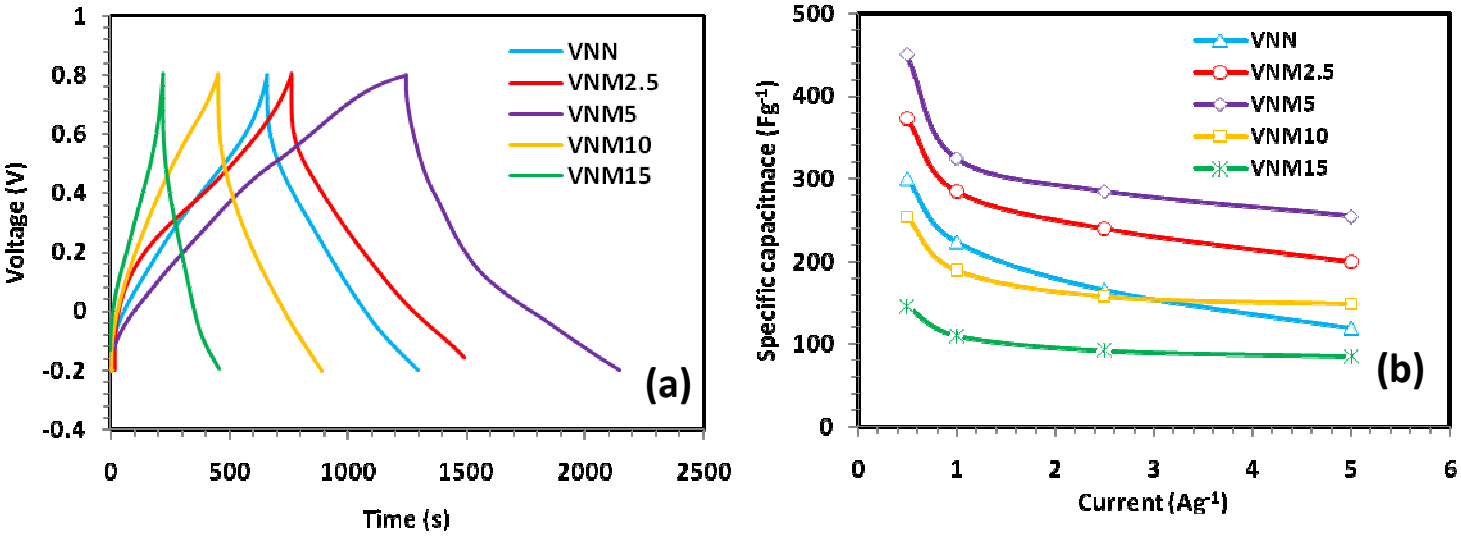

Fig. 7 (a) Charge/discharge curves for VNN, VNM2.5, VNM5, VNM10, and VNM15 measured at 0.5 Ag^{-1} (vs Ag/AgCl). (b) Variation of specific capacitance with different current densities.

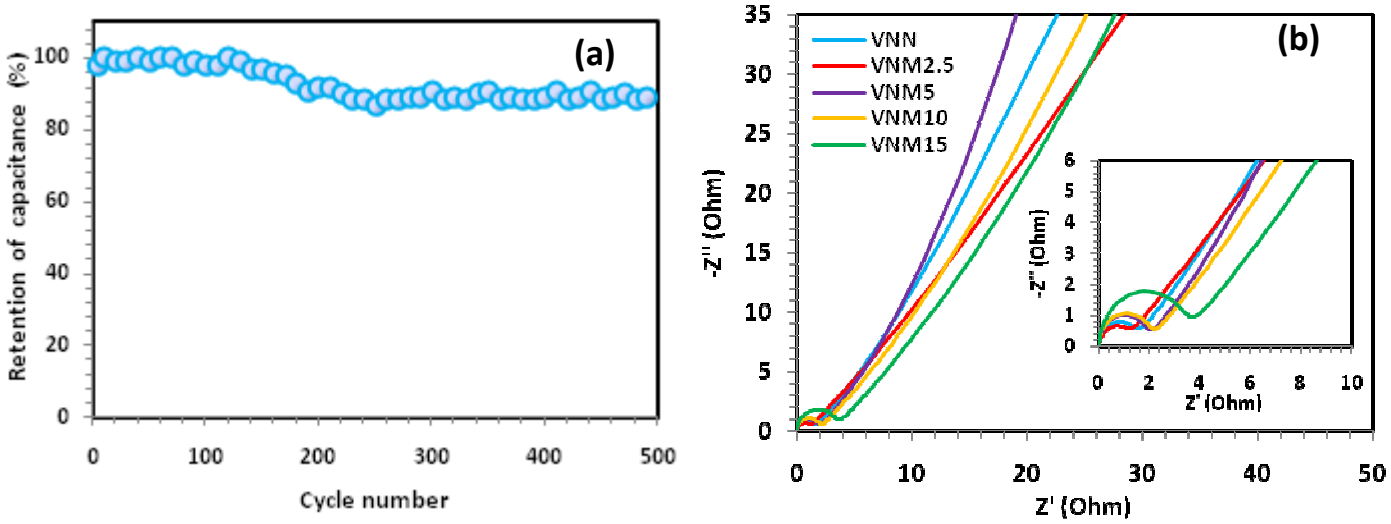

Fig. 8 (a) Cycling stability of VNM5 measured at 10 Ag^{-1} (vs Ag/AgCl). (b) Nyquist plots of the VNN, VNM2.5, VNM5, VNM10, and VNM15. Inset showing magnified view of high frequency region.

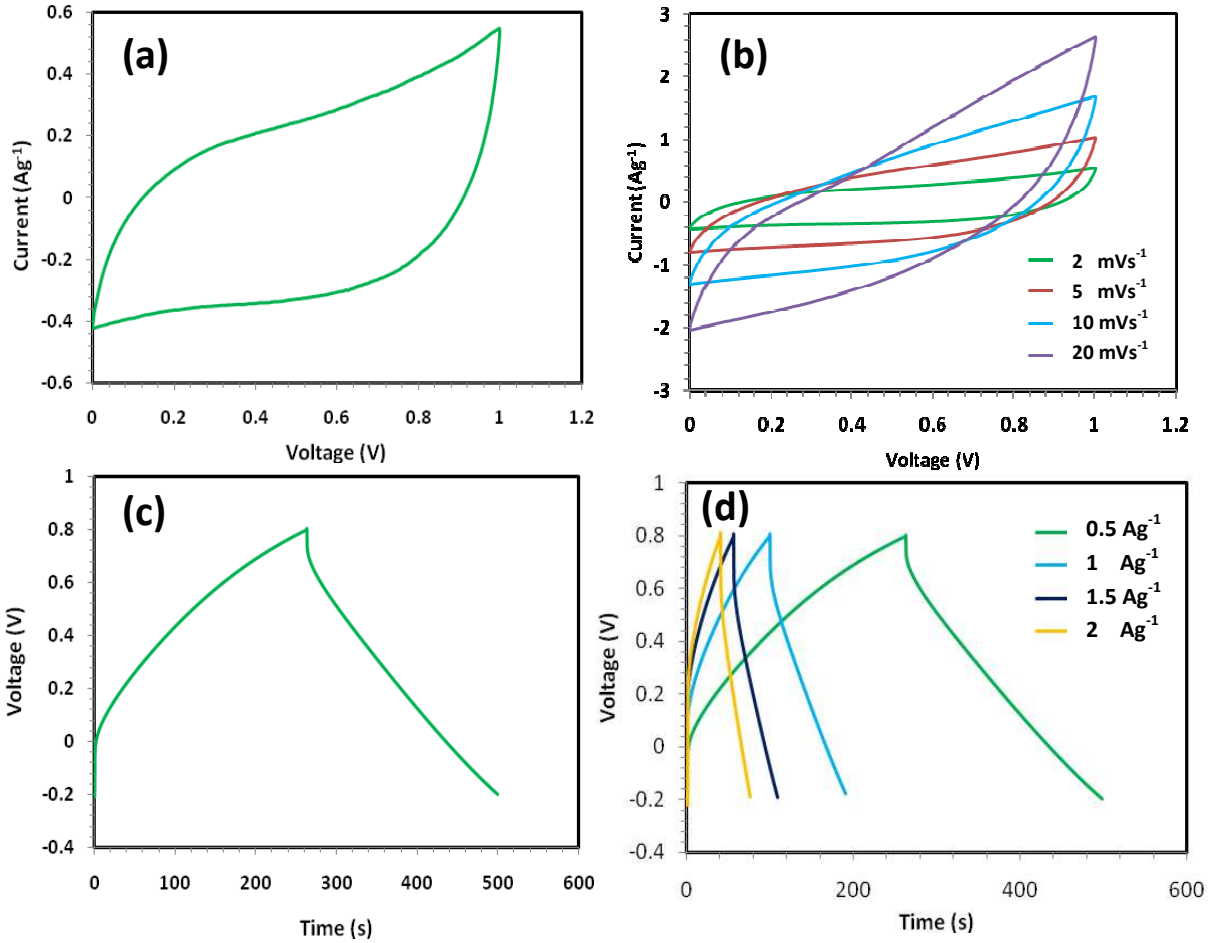

Fig. 9 CV curve of VNM5// AC asymmetric supercapacitor measured at $2mVs^{-1}$. (b) CV curves of VNM5// AC asymmetric supercapacitor measured at different scan rates. (c) GCD curve of VNM5// AC asymmetric supercapacitor measured at $0.5Ag^{-1}$ (d) GCD curves at different current densities.